Quantum enhanced measurement of an optical frequency comb

Y. Cai, J. Roslund, V. Thiel, C. Fabre, N. Treps

ARTICLE   OPEN

Check for updates

Quantum enhanced measurement of an optical frequency comb

Y. Cai [ID][1,2 ✉], J. Roslund[1], V. Thiel[3], C. Fabre[1] and N. Treps[1 ✉]

Measuring the spectral properties of an optical frequency comb is among the most fundamental tasks of precision metrology. In contrast to general single-parameter measurement schemes, we demonstrate here single shot multi-parameter estimation of an optical frequency comb at and beyond the standard quantum limit. The mean energy and the central frequency as well as the spectral bandwidth of ultrafast pulses are simultaneously determined with a multi-pixel spectrally resolved (MPSR) apparatus, without changing the photonics architecture. Moreover, using a quantum frequency comb that intrinsically consists of multiple squeezed states in a family of Hermite–Gaussian spectral/temporal modes, the signal-to-noise ratios of the multiple spectral parameters estimation can surpass the standard quantum limit. Combining our multi-pixel detection scheme and the multimode entangled resource could find applications in ultrafast quantum metrology and multimode quantum information processing.

INTRODUCTION

Optical frequency combs play a fundamental role in many types of precision measurements[1–3], including broadband spectroscopy[4,5], absolute frequency determination with optical clocks[6–9], and time–distance synchronization[10,11]. Measuring the spectral properties of an optical pulse is thus an important part of precision metrology[12–14]. The quantum-limited sensitivity for such measurements is dictated by the noise fluctuations present in a well-defined spectral mode[13,15], and the time and spectral separation has been performed experimentally[16,17]. For instance, the central frequency of optical pulses corresponds to the derivative of the line shape to be measured[18–20]. The measurement precision and signal-to-noise ratio (SNR) in these applications are generally limited by photon number fluctuations, which scale as $\sqrt{N}$, where N is the number of photons in the beam to be detected[21]. Optimally engineered squeezed states of light may be utilized to achieve a sensitivity beyond this quantum shot-noise limit[22], which has been widely applied in various measurements, such as laser interferometers[23–26], squeezing enhanced Raman spectroscopy[27], gravitational wave interferometry[28–31], optical magnetometry[32,33], laser beam pointing[34,35], biological sensing[36], distributed phase sensing[37], etc.

However, in order to characterize a system with several physical quantities, one often needs to measure multiple related parameters many times while modifying the corresponding set-up, which lacks flexibility. Here, we introduce a multimode approach for parallel estimation of multiple parameters of a light field, as well as quantum-enhanced metrology with incorporating an intrinsic multimode squeezed light[38]. In this work, we demonstrate a shot-noise limited measurement of multiple parameters characterizing the field of optical pulses of a frequency comb. To realize such parallel multiple parameter estimation, a multi-pixel spectrally resolved (MPSR) detector is developed. Post-processing the multichannel data of a single shot measurement, the central frequency, the mean energy and the spectral bandwidth of light

field are revealed. Also using this spectrally resolved apparatus, the full covariance matrix of a quantum frequency comb is reconstructed by simultaneously measuring all the spatially separated spectral components. Furthermore, the SNR of the central frequency and the mean energy as well as the spectral bandwidth measurements are enhanced with the appropriate use of an ultrafast squeezed light pulse[39,40]. Interestingly, two of the three parameters estimation, i.e., the mean energy and the spectral bandwidth, can surpass the quantum limit at the same time, then we thus demonstrate multiple parameters estimation of an optical frequency comb, i.e., beyond the shot-noise limit, without changing the photonics architecture. This method is general for realizing simultaneous interrogation of many parameters at and beyond the standard quantum limit, and could also be applied for other quantum information processing, e.g., quantum computing.

RESULTS

The quantum Cramér-Rao bound of spectral measurements

Let us consider the complex electric field of a single pulse of light, $\mathcal{E}(t)$, as the product of a mean amplitude and a specific pulse shape, $\mathcal{E}(t) = A_t u(t) \exp(i\omega_0 t)$, where $u(t)$ represents a specific time mode (i.e. a single pulse shape), ω_0 is the central frequency, and A_t is the complex amplitude. This pulse can be a single one or part of a train of pulses, such as an optical frequency comb, and this does not influence the following derivation as soon as the measurement device has a spectral resolution much lower than the comb repetition rate. The optical field can then simply be expressed in the frequency domain as

$$\mathcal{E}(\omega) = \mathcal{E}_0 E(\omega) = \mathcal{E}_0 \sqrt{N} u(\omega), \tag{1}$$

where $\mathcal{E}_0$ is a normalization constant chosen so that N represents the mean photon number, and $u(\omega)$ is the normalized spectral amplitude. For a mean-field mode with a gaussian spectral shape,
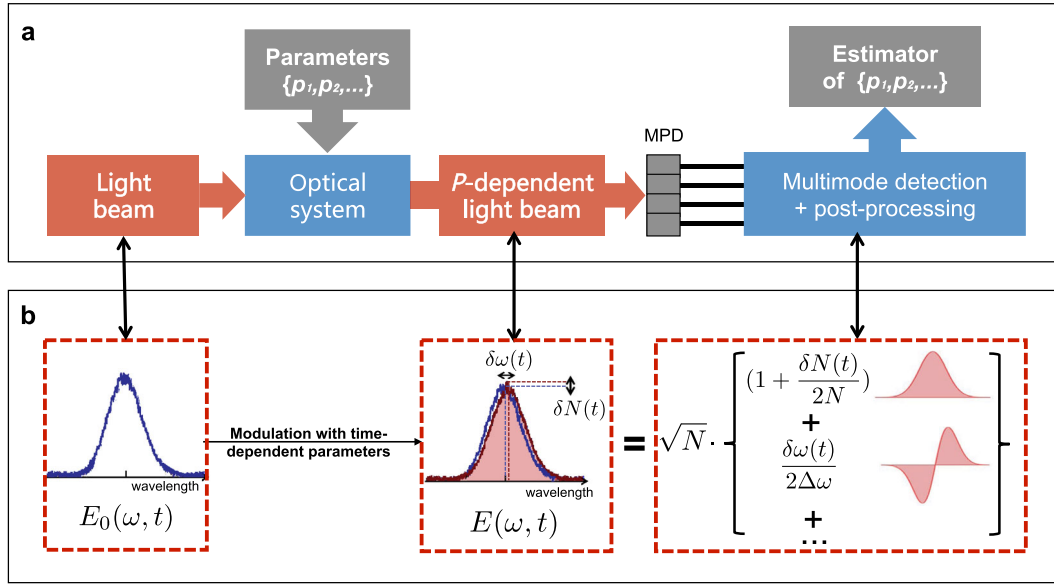
Fig. 1 Multi-parameters estimation scheme. a Parameter estimation with a multimode detection scheme. A light beam carrying the parameters is interrogated with a multi-pixel detector (MPD), and via post-processing the associated optical modes, multiple parameters can be simultaneously estimated. **b** Modal decomposition of a noisy optical pulse: physical noise parameters can be associated with different time/frequency modes. We represent here photon number and central frequency noise modes. Measurement of the associated modes can lead to Cramer-Rao bound limited sensitivity.

we have

$$u(\omega) = \sqrt{\frac{1}{\sqrt{2\pi}\Delta\omega}} \exp\left[\frac{-(\omega - \omega_0)^2}{4\Delta\omega^2}\right], \tag{2}$$

where ω_0 is the central frequency, $\Delta\omega$ is the spectral bandwidth, and $\int_{-\infty}^{\infty} u(\omega)u^*(\omega)d\omega$ is normalized to be unity. Thus to define such an optical pulse, the three parameters, i.e., N, ω_0, and $\Delta\omega$, need to be characterized.

Let us now consider that a small variation of the central frequency, $\delta\omega$, of the mean energy, $\delta\mathcal{N} = \mathcal{E}_0^2 \delta N$, and of the spectral bandwidth, $\delta(\Delta\omega)$ are present within the optical pulse. Then the electric field deviation can be expressed as

$$\delta E(\omega) \approx \frac{1}{2\sqrt{N}}\delta N u + \frac{\sqrt{N}}{2\Delta\omega}\delta\omega u_{CF} + \frac{\sqrt{N}}{\sqrt{2}\Delta\omega}\delta(\Delta\omega)u_{BD}. \tag{3}$$

The parameters corresponding to a displacement $\delta\mathcal{N}$ of the mean energy and $\delta\omega$ of the central frequency as well as $\delta(\Delta\omega)$ of the spectral bandwidth are carried by a specific mode or pulse shape. These normalized modes are respectively given by $u(\omega)$, $u_{CF}(\omega) = 2\Delta\omega \partial u(\omega)/\partial\omega = -\frac{\omega-\omega_0}{\Delta\omega}u(\omega)$, and $u_{BD} = \sqrt{2}\Delta\omega \partial u(\omega)/\partial\Delta\omega = \frac{(\omega-\omega_0)^2 - \Delta\omega^2}{\sqrt{2}\Delta\omega^2}u(\omega)$. Note that central frequency mode u_{CF} is orthogonal to the mean-field mode, while the bandwidth mode u_{BD} is not. This approach is very general to any parameter, and these mode-dependent parameters could be estimated with a multimode detection scheme, as illustrated in Fig. 1. An optical pulse perturbed by any type of noises can always be decomposed on a series of unperturbed modes, which carry corresponding time-dependent coefficients. These coefficients are associated with the variation of specific physical parameters. Their noise properties is ultimately governed by the quantum vacuum fluctuations in the corresponding modes, leading to the shot-noise limit in the measurement of these parameters. Hence, using squeezed light in some of these modes allows for a measurement with a precision that surpasses the shot-noise limit[34,41,42].

To describe the quantum limit in the measurement of these quantities, a full quantum representation of light is taken. Hence, the electric field operator is expressed as $\hat{E}(\omega) = \sum_i \hat{a}_i u_i(\omega)$, where $\hat{a}_i$ is the annihilation operator in the spectral mode $u_i(\omega)$, and

where we did omit the constant $\mathcal{E}_0$ for simplicity. In the case of coherent state illumination, the Cramér-Rao bound for the parameters δN, $\delta\omega$, and $\delta(\Delta\omega)$ in Eq. (3) is given by[18–20]

$$\delta N_{SQL} = \sqrt{N}, \tag{4}$$

$$\delta\omega_{SQL} = \frac{\Delta\omega}{\sqrt{N}}, \tag{5}$$

$$\delta(\Delta\omega)_{SQL} = \frac{\Delta\omega}{\sqrt{2}\sqrt{N}}, \tag{6}$$

where, δN_{SQL}, $\delta\omega_{SQL}$, and $\delta(\Delta\omega)_{SQL}$ are the minimum standard deviations for any estimator of the corresponding parameters, at the standard quantum limit.

In the more general case where the noise of the mode carrying the parameter is not at the shot-noise level, but still Gaussian, the Cramér-Rao bound is constrained by that noise:

$$\delta N_{CRB} = \sqrt{N}\sqrt{\langle\Delta^2\hat{x}_u\rangle}, \tag{7}$$

$$\delta\omega_{CRB} = \frac{\Delta\omega}{\sqrt{N}}\sqrt{\langle\Delta^2\hat{x}_{u_{CF}}\rangle}, \tag{8}$$

$$\delta(\Delta\omega)_{CRB} = \frac{\Delta\omega}{\sqrt{2}\sqrt{N}}\sqrt{\langle\Delta^2\hat{x}_{u_{BD}}\rangle}, \tag{9}$$

where $\hat{x}_u$, $\hat{x}_{u_{CF}}$, and $\hat{x}_{u_{BD}}$ are the optical amplitude quadrature of the modes u, u_{CF}, and u_{BD} respectively, defined as $\hat{x}_i = \hat{a}_i + \hat{a}_i^\dagger$, and $\Delta^2\hat{x}_i$ is the noise in the associated mode i. δN_{CRB}, $\delta\omega_{CRB}$, and $\delta(\Delta\omega)_{CRB}$ are the minimum standard deviations for any estimator with Gaussian noises. These Cramér-Rao bounds are taken as the measurement sensitivities for the experimentally measured parameters[18].

Model of the MPSR detection system

We now describe the model of the MPSR detection which is employed to reach the Cramér-Rao bound, as introduced in the previous section. This detection system is represented in Fig. 2, and has for input, in our case, a train of light pulses which carry
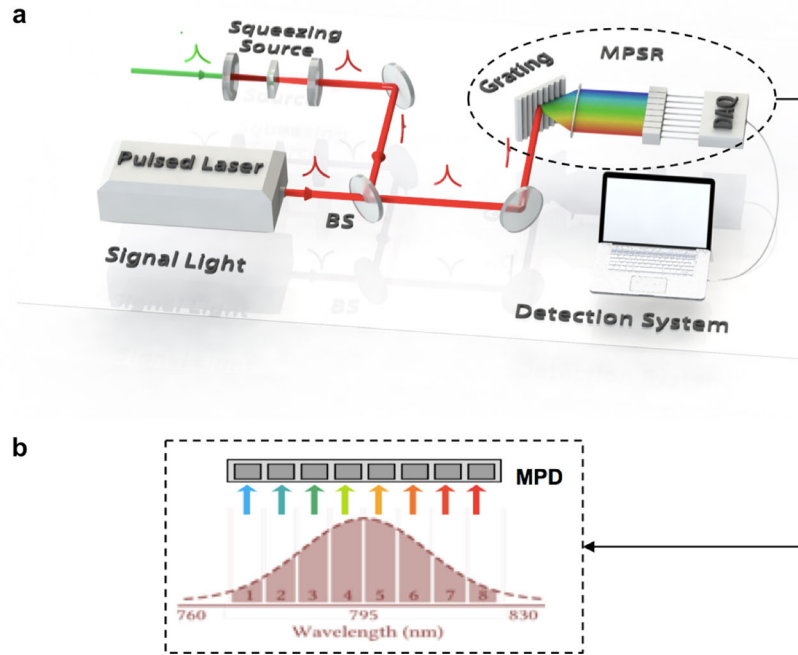
Fig. 2 Experimental set-up. a The simultaneous multimode measurement of frequency, energy and spectral bandwidth fluctuations within a laser field. All three parameters are modulated within the pulsed laser cavity. A multimode squeezing resource is then employed which allows enhancing the measurement of these quantity beyond the standard quantum limit. This is accomplished by mixing the squeezer with the laser field via a strongly reflective beam splitter. The resultant synthetic beam is spectrally dispersed and imaged onto a photodiode array after passing a micro-lenses array. The photocurrents corresponding to each of the eight pixels are transferred to a computer for post-processing. BS beam splitter, 10/90; grating has 93% efficiency; MPSR homemade multi-pixel spectrally resolved detector. **b** The corresponding spectral bins of equivalent width are simultaneously interrogated with an eight-pixel photodiode array. MPD multi-pixel detector.

the information to be extracted. These pulses are diffracted on a grating and the different color components are then detected simultaneously by a one-dimension photodiode array. Hence, the modes effectively detected by the multi-pixel array, which we call the pixel modes and write also $\{u_i\}$ for simplicity, are the normalized spectral slices of the mean field of the intense beam shining on the detector pixels. Thus, these pixel modes, $\{u_i\}$, define the measurement basis.

In order to recover the mode which carries a given parameter, for instance the central frequency, one can implement a real linear basis change on these measured photocurrents. Let us call $\{v_s\}$ the mode we want to recover, associated with annihilation operator $\hat{a}_s$. We approximate this mode from the pixel modes:

$$\hat{a}_s \simeq \hat{a}_m = \frac{\sum_i m_i \hat{a}_i}{\eta}, \tag{10}$$

where the projection coefficients, $m_i = \int u_i^*(\omega) v_s(\omega) d\omega$ and the detection efficiency, $\eta = \sqrt{\sum_i m_i^2}$. We assume, as is the case both in the theoretical description and in the experiment, that all the m_i are real, meaning that the spectral phase of the mode v_s is the same as the one of the pixel modes. Note that one can easily include this possible phase variation in the calculation, but we omit it for simplicity. Hence, if the detection efficiency η is equal to 1, the mode $\hat{a}_s$ is perfectly recovered and the measurement sensitivity exactly reaches the Cramér-Rao bound[41]. In the general case, the quality of the approximation between the signal mode $\hat{a}_s$ and the measured mode $\hat{a}_m$ depends ultimately on the number of pixels and on the filling factor of these pixels onto the photodiode array relative to the pixel modes of the optical spectrum to be measured.

More specifically, because we aim at measuring a variation of the mean field as defined in Eq. (3), we can consider the small variations of the measured intensity on each pixel mode relative to the mean power. As the mean field is intense, one can write that the variation of $\hat{I}_i = \hat{a}_i^\dagger \hat{a}_i$ is equal to $\delta \hat{I}_i = a_i \delta \hat{x}_i$ where a_i is the

amplitude of the field in the ith pixel mode $\hat{a}_i$, considered as real without loss of generality, and $\delta \hat{x}_i = \hat{x}_i - \langle \hat{x}_i \rangle$ is the fluctuation quadrature operator. Hence, post-processing the measured intensity using Eq. (10) one can directly reconstruct $\delta \hat{x}^m = \frac{1}{\eta} \sum_i m_i \frac{\delta I_i}{a_i}$ and access the fluctuations of mode $\hat{a}_m$. In the case where $\eta = 1$, the multi-pixel detection system is able to estimate the parameter carried on a specific mode, reaching the Cramér-Rao bound of Eqs. (7) and (8). If the modes are squeezed on the amplitude quadrature $((\delta \hat{x}^m)^2 < 1)$, the sensitivity increases beyond the shot-noise limit, allowing for a smaller value of the corresponding parameters to be measured. The case $\eta < 1$ is equivalent to a reduced efficiency of the detection, and leads to a corresponding reduced sensitivity.

Furthermore, using conventional single-pixel detection methods, such orthogonal parameters cannot be simultaneously measured. However, using the MPSR, one may choose several on-demand spectral modes to characterize and apply the corresponding post-processing simultaneously. The MPSR allows arbitrary real basis change on the original multi-pixel data. Thus, this methodology enables parallel parameter estimation via post-processing without changing the optical set-up.

Experimental set-up and shot-noise limited measurement

Our experimental set-up is displayed in Fig. 2. A train of ~100 fs optical pulses centered at 795 nm with a repetition rate of 76 MHz propagates through a weakly transmitting beam splitter. In practice, the center wavelength of the spectrum is shifted by modulating at a high frequency the tilt of a mirror inside the pulsed laser cavity. The modulation is done at $f_m = 1.5$ MHz in order to avoid the technical noise of the laser field and ensuring that the measurement is done at the shot-noise limit. The optical beam is spectrally dispersed by a high efficiency grating and imaged onto an eight-pixel photodiode array. To avoid the gaps in between pixels of the
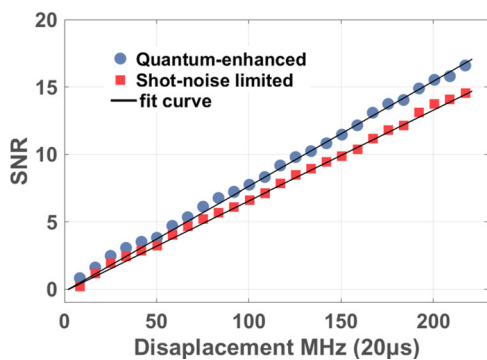
Fig. 3 Signal-to-noise ratio (SNR) measurements. Measurement of the central frequency displacement that is induced inside the laser cavity. The blue and the red lines are the SNRs for the shot-noise limited and quantum-enhanced cases, respectively. All the measurements are implemented at 1.5 MHz modulation sideband where all the classical noises could be ignored. All the data are only corrected for electric dark noise. The measurement time is taken to be 20 μs for each measurement, which is defined by the bandwidth (50 kHz) of the low-pass filter. The error bar for each point above is less than 2%, as the system is well locked and many events are used in the measurements. These quantities of the error bars are small, and are thus not drawn for clarity.

photodiode array, we use a micro-lenses array to focus the eight-color components on each pixel. The low-noise amplifiers of the photodiodes have a bandwidth of about 10 MHz. The photocurrents from the individual pixels are then individually demodulated at the modulation frequency f_m and fed into a data acquisition system after passing through a 50 kHz low-pass filter.

Once all the photocurrents are acquired by the computer, we can calculate the signal and noise of different spectral modes as defined in Eq. (10). The coefficients m_i in Eq. (10) are calculated from the low-frequency output of the MPSR, which gives the spectral amplitude of the mean field, and the predicted modes associated with each parameter. In order to retrieve the sensitivity, we vary the modulation depth in the laser cavity and calculate for each modulation the SNR using 1000 data points at a sampling rate of 20 kHz. It is represented in Fig. 3 with the particular example of the derivative mode associated with the central frequency fluctuations. The blue curve corresponds to the obtained sensitivity for coherent input light.

In order to calibrate the sensitivity and the measurement, we evaluate its properties. On the photodiode array, the field is spread over a detected bandwidth of 8.8 nm full-width half-maximum (FWHM), $\Delta\omega_{FWHM} = 2\sqrt{2\ln 2}\Delta\omega$, and contains a photon flux of $N_p \simeq 4 \times 10^{16}$ photons s^{-1} (which corresponds to ~10 mW of total optical power). These experimental values lead to a shot-noise limited sensitivity as defined in Eq. (8) of $\delta\omega_{SQL} \approx$ 55.7 kHz Hz$^{-\frac{1}{2}}$, which is much smaller than the 76 MHz spacing between the comb tooth. Considering the quantum efficiency of the photodiodes, the optical losses and limited number of pixels that induce a measured non-perfect mode mismatch with the ideal spectral mode, the global efficiency in intensity η^2 is evaluated as 70%, and the practical sensitivity is thus $\delta\omega_{meas.} \approx$ 66.5 kHz Hz$^{-\frac{1}{2}}$. The measurement time, induced by the low-pass filter, is 20 μs, thus experimentally, the actual sensitivity presented in Fig. 3 is calculated to be 14.9 MHz for each measurement event.

The quantum frequency comb and quantum-enhanced spectrometer

In this section, we show how the MPSR detector can be utilized with multimode squeezed vacuum to simultaneously measure orthogonal parameters of the optical field with a precision that surpasses the shot-noise limit.

Multimode quantum light is generated by an optical parametric oscillator (OPO) synchronously pumped by the second harmonic of a femtosecond mode-locked laser, as shown in Fig. 2. The quantum state consists of multimode squeezed vacuum on a basis of time/frequency modes that resemble closely the modes obtained by expansion of the field in Eq. (3)[39]. To characterize that quantum state, we use two MPSR detectors in a spectrally resolved homodyne detection scheme to simultaneously record the quadrature operators in the frequency band basis. We use this information to reconstruct the eight-partite covariance matrix of the quantum frequency comb, both in amplitude and phase, as depicted in Fig. 4a. Note that the total interrogation time to obtain the full covariance matrix is a few seconds with vacuum squeezing locked on the amplitude or phase quadrature (see "Methods" for details). This measurement technique is also promising for quantum information processing, which requires simultaneous interrogation of the various entangled parties[43–46].

The full covariance matrix contains all the quantum correlations of the multimode gaussian quantum resource. Using Bloch Messiah decomposition[47] we extract from the covariance matrix a set of orthogonal squeezed modes, which happen to be very similar to a set of Hermite–Gaussian spectral shapes in the frequency domain (corresponding to pulse shapes in the time domain). The leading four squeezed eigenmodes are presented in Fig. 4b, which are respectively squeezed by −2.9, −2.2, −1.7, and −1.4 dB, corrected for electrical dark noise. Note that the odd-order eigenmodes are squeezed on the amplitude while the even-order ones are squeezed on the phase quadrature. Here the squeezing levels are mainly limited by the quantum efficiency of the photodiode array (~80% quantum efficiency, Hamamatsu S8558), but one could see that the mean-field mode and the central frequency mode as well as the bandwidth mode are close to the leading three eigenmodes which are all significantly squeezed.

In order to implement the quantum-enhanced measurement, the quantum frequency comb generated by the OPO is then combined with the optical field coherently on a weakly transmitting beam splitter. In this way, the generated beam carries the mean field of the original comb, yet with the quantum fluctuation of the quantum frequency comb. Therefore, the synthetic beam consists on a multimode optical field that carries the parameters to be measured with a noise that is either below or above shot noise because of quadrature squeezing. In practice, as the beam splitter reflectivity is about 90%, the squeezed state undergoes about 10% losses. Experimentally multiple optical phases have to be locked together. The OPO has to be seeded in order to be locked on amplification, i.e., the resulting eigenmodes are squeezed on the amplitude quadrature. Additionally, the strong signal field and the squeezed vacuum have to be locked together; this is achieved by locking the signal to the seed. The measurement with quantum vacuum is then performed employing a fast mechanical shutter which blocks the seed beam while holding the electrical locks, allowing for a 100 ms measurement window before the shutter opens and the locks are resumed. Once data are acquired, the analysis is then performed in the exact same way as in the previous section.

Reconstructing the mode associated with central frequency fluctuations u_d, we see that the SNR is enhanced by ~15% with respect to the standard shot-noise sensitivity. As seen in Fig. 3, we recover a higher response to the modulation depth compared to the previous case. By computing the ratio between the slopes of the blue (shot-noise limited) and red (quantum enhanced) curves, the quantum-enhanced sensitivity is $\delta\omega_{Quan} \approx$ 57.8 kHz Hz$^{-\frac{1}{2}}$, thus with 20 μs measurement time, the actual quantum-enhanced sensitivity is 12.9 MHz.

The MPSR is a flexible platform that allows for simultaneous extraction of multiple orthogonal modes by post-processing. In addition to quantifying the frequency fluctuations, variations in the mean energy and the spectral bandwidth of the light field
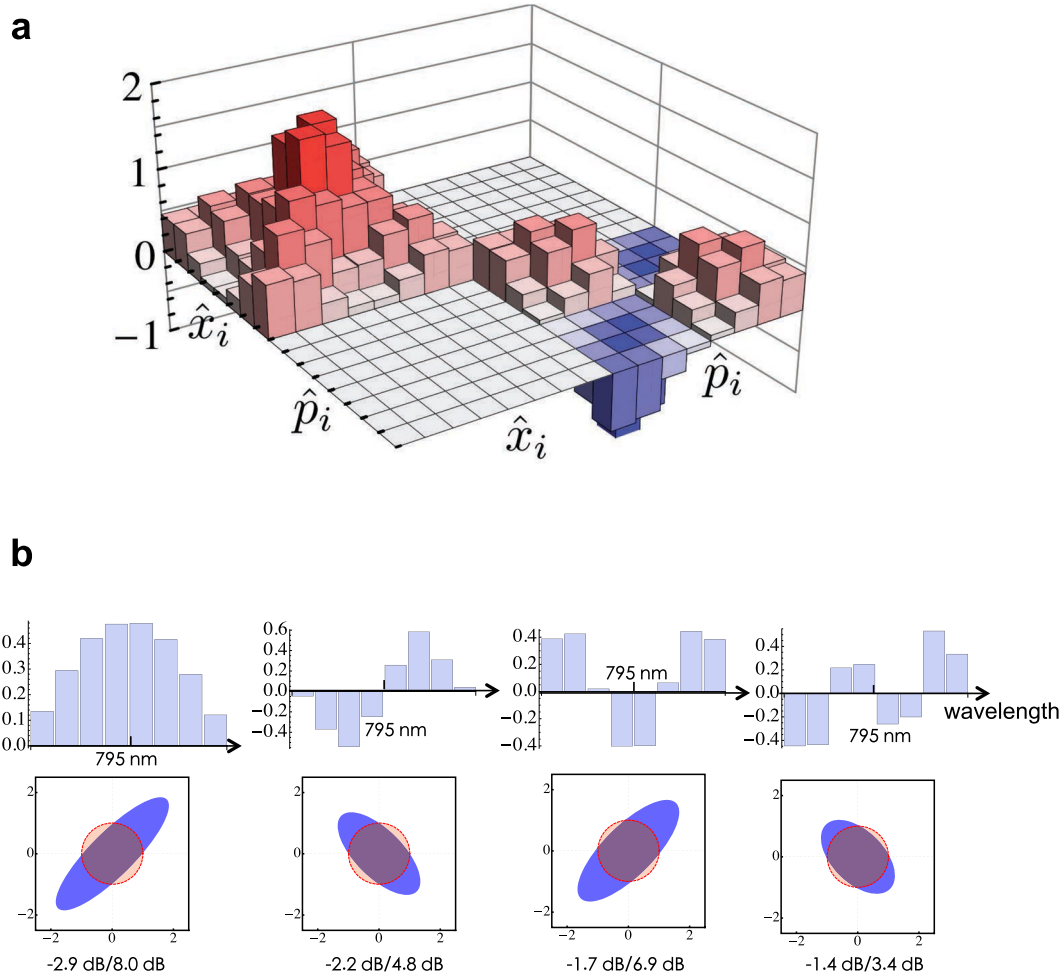
Fig. 4 The quantum state of the multimode quantum resource. a Eight-partite full covariance matrix of the multimode quantum resource via multi-pixel homodyne measurement. All the amplitude or phase quadrature of different color components, $\hat{x}_i$ or $\hat{p}_i$, are simultaneously interrogated, and the spectrum of the local oscillator is divided into eight frequency bands of equivalent width. The covariance matrix elements are defined as $\frac{1}{2}\langle \hat{\zeta}_i\hat{\zeta}_j + \hat{\zeta}_j\hat{\zeta}_i \rangle - \langle \hat{\zeta}_i \rangle \langle \hat{\zeta}_j \rangle$, where $\hat{\zeta}_i = \hat{x}_i, \hat{p}_i$. The shot-noise contribution has been subtracted from the diagonal for better visibility, and the noise level is normalized to vacuum noise (i.e. shot noise is equal to 1). Note that our squeezer presents no amplitude-phase cross-correlation, hence the corresponding parts in the full covariance matrix are all zero. **b** The squeezing values of the four leading spectral modes (up) and the corresponding squeezing ellipse in quadrature phase space. The red circles represent the shot noise, and the odd-order and even-order modes are squeezed in amplitude and phase quadrature, respectively. Both (**a** and **b**) were only corrected for electrical dark noise.

are simultaneously obtained by reconstructing an alternative photocurrent superposition (i.e., the sum of the individual photocurrents which corresponds to the mean-field mode). In practice, the modulation of the center frequency within the laser cavity also causes an energy variation and an spectral bandwidth variation. According to Eq. (3), all variations in energy, frequency, and spectral bandwidth can be retrieved by post-processing the mean-field mode and the central frequency mode as well as the bandwidth mode, respectively, seen in Fig. 5a. As seen in Fig. 5b, c, while the sensitivity for determining frequency deviations is enhanced with a squeezing resource, the sensitivity for the measurements of energy and bandwidth fluctuations are degraded with respect to the shot-noise limit. This is due to the fact that the modes corresponding to these two spectral structures are squeezed in opposite quadratures (i.e., the frequency mode is squeezed while the mean-field mode and the bandwidth mode are anti-squeezed). Note that the results for the central frequency are similar to that in the previous single-parameter case in Fig. 3. However, as seen in Fig. 5d, acting on the locking system one can change which parameter is to be squeezed, and switch to a synthetic beam whose energy

and bandwidth parameters estimation are enhanced simutaneously. The corresponding shot-noise limited sensitivity of mean energy shifts is $\delta N_{SQL} \approx 2 \times 10^8$ photons $s^{-\frac{1}{2}}$, and with considering the global efficiency, the practical sensitivity is $\delta N_{mesa} \approx 1.7 \times 10^8$ photons $s^{-\frac{1}{2}}$. According to the SNR ratio in Fig. 5, the quantum-enhanced sensitivity for the mean energy shift is $\delta N_{Quan} \approx 1.4 \times 10^8$ photons $s^{-\frac{1}{2}}$, which is ~19% improved compared to the one with shot-noise limited. For a measurement time of 20 μs, the actual sensitivities are 7.5×10^5 photons and 6.1×10^5 photons for shot-noise limited and quantum-enhanced, respectively. Similarly, the shot-noise limited sensitivity for the spectral bandwidth are $\delta(\Delta\omega)_{SQL} \approx 39.4$ kHz Hz$^{-\frac{1}{2}}$, and considering the global efficiency, the actual sensitivity is $\delta(\Delta\omega)_{SQL} \approx 47.1$ kHz Hz$^{-\frac{1}{2}}$. The quantum-enhanced sensitivity is $\delta(\Delta\omega)_{Quan} \approx 33.4$ kHz Hz$^{-\frac{1}{2}}$, which is ~29% improved compared to the shot-noise limited one. And for a measurement time of 20 μs, the actual sensitivities are 10.5 and 7.46 MHz for shot noise and quantum-enhanced light, respectively. Note that as the central frequency mode is orthogonal to the energy mode, our MPSR scheme has no fundamental limit to realize all the three
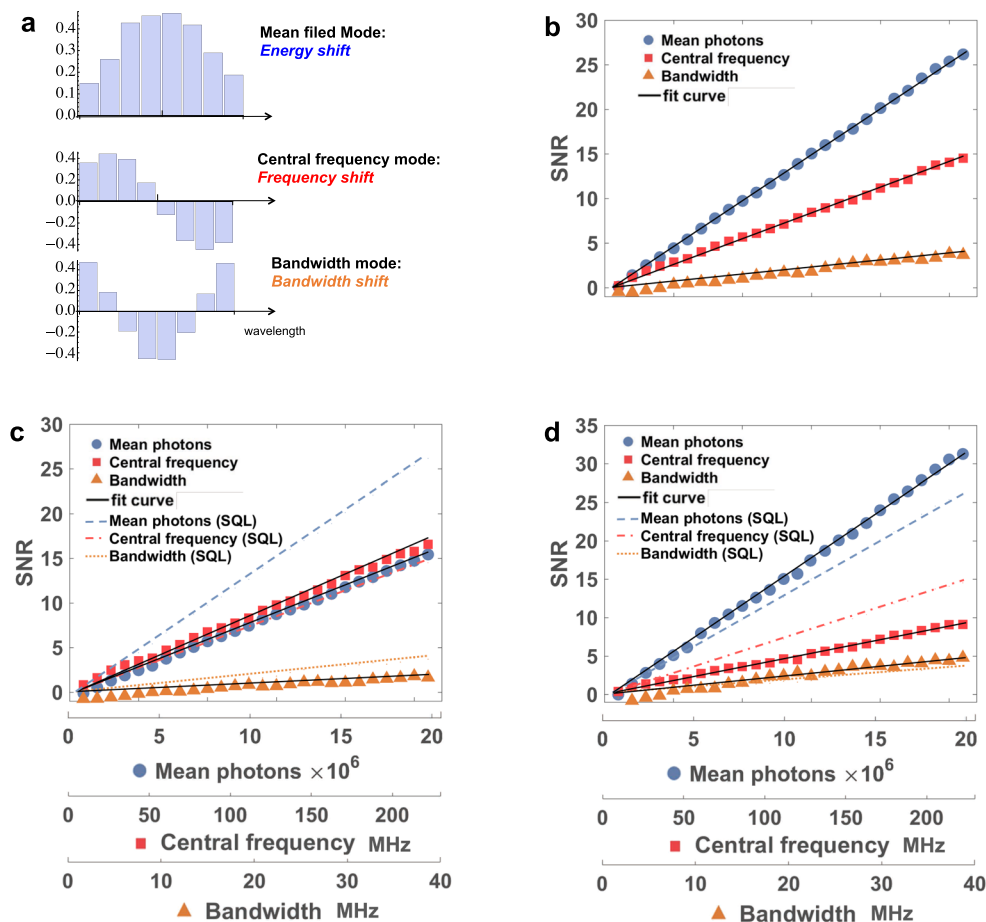
Fig. 5 Signal-to-noise ratio (SNR) measurements of multi-parameters. a Experimental detection modes corresponding to the mean field (top), the central frequency mode (middle), and the bandwidth mode (bottom), which are reconstructed based on the mean field. **b–d** SNRs for mean field (blue curves) and central frequency mode (red curves) as well as spectral bandwidth mode (orange curves) while increasing the modulation depth of displacement, **b** when the other port of the beam splitter is vacuum, **c** quantum frequency comb with a squeezed central frequency mode, and (**d**) quantum frequency comb with a mean field and a bandwidth mode squeezed at the same time. The measured standard quantum limit (SQL) presented in (**b**) is added in (**c** and **d**) (dashed lines). As the system is well locked and many events are used in the measurements, error bars for each SNR point are small (<2%), and are thus not drawn for clarity.

parameters estimation beyond the standard quantum limit simultaneously, depending only on the squeezing resource.

DISCUSSION

The present work provides a proof of principle for the ability to exceed the standard quantum limit in the measurement of frequency and energy as well as spectral bandwidth fluctuations within an optical frequency comb. Importantly, the use of a multiplexed detection device is general and enables the simultaneous estimation of multiple parameters characterizing the light pulses. The three parameters, central frequency and mean energy as well as spectral bandwidth, are measured in parallel at the shot-noise limit. Furthermore, using the quantum frequency comb, which is intrinsically multimode squeezed, we improve the sensitivity of the three parameters beyond the shot-noise limit by 19%, 15%, and 29%, for mean energy, central frequency, and spectral bandwidth, respectively. Interestingly, there is one configuration, where two of the three parameters, i.e., the mean energy and the spectral bandwidth, estimation can be quantum enhanced at the same time.

Notably, appropriate linear combinations of the multiple photocurrents of the wavelength-multiplexed detection have also revealed variations in the field bandwidth, temporal jitter, and overall phase[15]. This fact suggests a tremendous flexibility in the

use of multimode detection for the interrogation of multi-dimensional light fields. Moreover, multimode measurement-based quantum computing and multipartite quantum secure communications could also be implemented with a MPSR homodyne detection scheme[48,49]. Applying the present multi-pixel detection scheme together with a controllable non-Gaussian operation such as photon subtraction[50] is a promising way to realize quantum advantage.

METHODS

Multi-pixel homodyne detection

To realize simultaneously interrogating the multimode quantum correlations, the multi-pixel homodyne detection is applied, which is desired for quantum information processing[48]. The multipartite frequency structure of ultrafast pulse trains provides a rich platform for the generation of squeezed modes of various spectral shapes[39]. The second harmonic of a 76 MHz pulse train delivering ~120 fs pulses centered at 795 nm synchronously pumps a below-threshold OPO. The squeezed vacuum output of this synchronously pumped OPO (SPOPO) has been demonstrated to consist of a multimode squeezed state in which the spectral structure of each mode closely approximates a Hermite–Gaussian progression. For instance, the second squeezed mode of the series provides a close approximation to the derivative of the original spectral field, which is the optimal mode for identifying frequency variations[15].
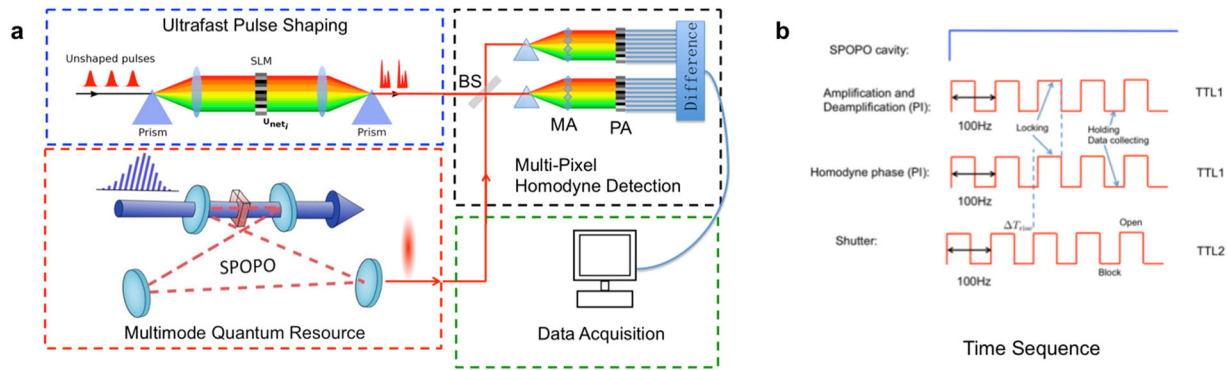
Fig. 6 Simultaneous measurement regime with multi-pixel Homodyne detection. a The multimode quantum resource is generated via a synchronously pumping an optical parametric oscillator (SPOPO). The local beam of homodyne detection could apply pulse shaping technique to access on-demand pulse shapes, which is not yet used for constructing covariance matrix. The two beams, going through a balanced beam splitter (BS), are dispersed by a pair of dispersive optics, and each color injects on the corresponding pixel of the the photodiode array (PA). To eliminate the loss induced by the gaps between the pixels of PA, a pair of micro-lens arrays (MA) is set in front of the PA. **b** Time sequence for locking and data acquisition.

The multimode quantum correlations of the quantum resource are measured simultaneously via multi-pixel balanced homodyne detection. This spectrally resolved apparatus provides many individual homodyne detecting different colors of pulses at the same time, which enables to collect the quantum correlations among all channels simultaneously. The full covariance matrix of the multimode gaussian state can then be reconstructed with the measured quantum correlations. Importantly, the simultaneous homodyne measurement is required in multimode quantum information processing[48] and allows for the present parallel parameter estimation within multimode.

As seen in Fig. 6a, the multimode quantum resource[39], and the local oscillator are balanced mixed with the beam splitter. Different from general homodyne detection, after the 50/50 beam splitter, the two balanced arms pass through an optical dispersion device, and all the frequency components are thus simultaneously interrogated via the homemade multi-pixel detection apparatus. To reconstruct the full covariance matrix, amplitude and phase quadrature correlations are collected by two single measurements, while locking the relative phase between the signal and the local light at 0 and $\pi/2$, respectively.

Experimentally, for dispersing the light, a pair of optical gratings with the efficiency of 93% are used. The homemade multi-pixel apparatus has ~80% detection efficiency, 10 MHz detection bandwidth, and commercial photodiode arrays (~80% quantum efficiency, Hamamasu S8558) are used, as well as microlensarray is applied to focus the dispersed light onto the sensing pixels of the photodiode arrays. The homodyne visibility is 94%.

The data are interrogated with a vacuum squeezing locking. As seen in Fig. 6b, the time sequence is trigged with a two-channel high precision signal generator, which generates TTL1 and TTL2 with a fixed relative time difference of a few milliseconds. A fast mechanical shutter is used to control the seed beam of SPOPO, and its on-off frequency is set to be 10–100 Hz. The both locking of the cavity and amplification (deamplification) is on with seed beam, and the covariance data of SPOPO are collected while the seed beam is blocked and the locking is hold.

To reconstruct the covariance matrix, the quantum correlations are measured via the multi-pixel homodyne detection. All the difference signal of each pair of the frequency pixels in the multi-pixel homodyne detection are measured simultaneously, and the difference of the ith pair of detector pixels represent the quadrature value in the ith frequency band, expressed as below,

$$\hat{I}_i^- = 2|a_i|^2 \hat{o}_i, \qquad (11)$$

where a_i is the amplitude of the ith frequency band of the local oscillator, and $\hat{o}_i$ represents the corresponding quadrature of the signal field. The covariance matrix with amplitude and phase quadrature correlations are reconstructed by calculating the variances of combined difference signals. To construct the full covariance matrix, the correlations terms are defined,

$$\langle \hat{o}_i \hat{o}_j \rangle = \frac{\langle \hat{I}_i^- \hat{I}_j^- \rangle}{4|a_i|^2 |a_j|^2}. \qquad (12)$$

Importantly, the leading three squeezed modes of the series provides a close approximation to the mean-field mode and the central frequency mode as well as the bandwidth mode, which identify energy, central frequency, and spectral width variations. Hence, combining the multimode squeezed states and the multichannel detector allows for parallel estimation of corresponding parameters beyond the standard quantum limit.

DATA AVAILABILITY
All the data and calculations that support the findings of this study are available from the corresponding author upon reasonable request.

REFERENCES
1. Udem, T., Holzwarth, R. & Hänsch, T. W. Optical frequency metrology. *Nature* **416**, 233–237 (2002).
2. Cundiff, S. T. & Ye, J. Femtosecond optical frequency combs. *Rev. Mod. Phys.* **75**, 325 (2003).
3. Ludlow, A. D., Boyd, M. M., Ye, J., Peik, E. & Schmidt, P. O. Optical atomic clocks. *Rev. Mod. Phys.* **87**, 637 (2015).
4. Thorpe, M. J., Moll, K. D., Jones, R. J., Safdi, B. & Ye, J. Broadband cavity ringdown spectroscopy for sensitive and rapid molecular detection. *Science* **311**, 1595–1599 (2006).
5. Diddams, S. A., Hollberg, L. & Mbele, V. Molecular fingerprinting with the resolved modes of a femtosecond laser frequency comb. *Nature* **445**, 627–630 (2007).
6. Rosenband, T. et al. Frequency ratio of Al$^+$ and Hg$^+$ single-ion optical clocks; metrology at the 17th decimal place. *Science* **319**, 1808–1812 (2008).
7. Diddams, S. A. et al. An optical clock based on a single trapped ^{199}Hg$^+$ ion. *Science* **293**, 825–828 (2001).
8. Bloom, B. J. et al. An optical lattice clock with accuracy and stability at the 10^{-18} level. *Nature* **506**, 71–75 (2014).
9. Katori, H. Optical lattice clocks and quantum metrology. *Nat. Photonics* **5**, 203–210 (2011).
10. Coddington, I., Swann, W., Nenadovic, L. & Newbury, N. Rapid and precise absolute distance measurements at long range. *Nat. Photonics* **3**, 351–356 (2009).
11. van den Berg, S. A., Persijn, S. T., Kok, G. J. P., Zeitouny, M. G. & Bhattacharya, N. Many-wavelength interferometry with thousands of lasers for absolute distance measurement. *Phys. Rev. Lett.* **108**, 183901 (2012).
12. Bartels, A., Oates, C. W., Hollberg, L. & Diddams, S. A. Stabilization of femtosecond laser frequency combs with subhertz residual linewidths. *Opt. Lett.* **29**, 1081–1083 (2004).
13. Haus, H. A. & Lai, Y. Quantum theory of soliton squeezing: a linearized approach. *J. Opt. Soc. Am. B* **7**, 386 (1990).
14. Haus, H. A. & Mecozzi, A. Noise of mode-locked lasers. *IEEE J. Quantum Electron.* **29**, 983 (1993).
15. Schmeissner, R., Roslund, J., Fabre, C. & Treps, N. Spectral noise correlations of an ultrafast frequency comb. *Phys. Rev. Lett.* **113**, 263906 (2014).
16. Donohue, J. M. et al. Quantum-limited time-frequency estimation through mode-selective photon measurement. *Phys. Rev. Lett.* **121**, 090501 (2018).

17. Ansari, V., Brecht, B., Gil-Lopez, J., Donohue, J. M., Řeháček, J., Hradil, Z., ... & Silberhorn, C. Achieving the ultimate quantum timing resolution. *PRX Quantum* **2**, 010301 (2021).

18. Pinel, O. et al. Ultimate sensitivity of precision measurements with intense Gaussian quantum light: a multimodal approach. *Phys. Rev. A* **85**, 010101 (2012).

19. Jian, P., Pinel, O., Fabre, C., Lamine, B. & Treps, N. Real-time displacement measurement immune from atmospheric parameters using optical frequency combs. *Opt. Express* **20**, 27133–27146 (2012).

20. Thiel, V., Roslund, J., Jian, P., Fabre, C. & Treps, N. Quantum-limited measurements of distance fluctuations with a multimode detector. *Quantum Sci. Technol.* **2**, 034008 (2017).

21. Bachor, H. A. & Ralph, T. C. *A Guide to Experimental in Quantum Optics* 2nd edn (Wiley-VCH, New York, 2004).

22. Caves, C. M. Quantum-mechanical noise in an interferometer. *Phys. Rev. D* **23**, 1693 (1981).

23. Xiao, M., Wu, L. A. & Kimble, H. J. Precision measurement beyond the shot-noise limit. *Phys. Rev. Lett.* **59**, 278 (1987).

24. Grangier, P., Slusher, R. E., Yurke, B. & LaPorta, A. Squeezed- light-enhanced polarization interferometer. *Phys. Rev. Lett.* **59**, 2153 (1987).

25. Eberle, T. et al. Quantum enhancement of the zero-area Sagnac interferometer topology for gravitational wave detection. *Phys. Rev. Lett.* **104**, 251102 (2010).

26. Steinlechner, S., Rohweder, N.-O., Korobko, M. & Töyrä, D. Mitigating mode-matching loss in nonclassical laser interferometry. *Phys. Rev. Lett.* **121**, 263602 (2018).

27. Michael, Y., Bello, L., Rosenbluh, M. & PeÕer, A. Squeezing-enhanced Raman spectroscopy. *npj Quantum Inf.* **5**, 81 (2019).

28. The LIGO Scientific Collaboration. A gravitational wave observatory operating beyond the quantum shot-noise limit. *Nat. Phys.* **7**, 962–965 (2011).

29. The LIGO Scientific Collaboration. Enhanced sensitivity of the LIGO gravitational wave detector by using squeezed states of light. *Nat. Photonics* **7**, 613–619 (2013).

30. Grote, H. et al. First long-term application of squeezed states of light in a gravitational-wave observatory. *Phys. Rev. Lett.* **110**, 181101 (2013).

31. Tse, M. et al. Quantum–enhanced advanced LIGO detectors in the era of gravitational-wave astronomy. *Phys. Rev. Lett.* **123**, 231107 (2019).

32. Wolfgramm, F. et al. Squeezed-light optical magnetometry. *Phys. Rev. Lett.* **105**, 053601 (2010).

33. Li, B. B. et al. Quantum enhanced optomechanical magnetometry. *Optica* **5**, 850–856 (2018).

34. Treps, N. et al. A quantum laser pointer. *Science* **301**, 940–943 (2003).

35. Pooser, R. C. & Lawie, B. Ultrasensitive measurement of microcantilever displacement below the shot-noise limit. *Optica* **2**, 393–399 (2015).

36. Taylor, M. A. et al. Biological measurement beyond the quantum limit. *Nat. Photonics* **7**, 229–233 (2013).

37. Guo, X. et al. Distributed quantum sensing in a continuous-variable entangled network. *Nat. Phys.* **16**, 281–284 (2020).

38. Fabre, C. & Treps, N. Modes and states in quantum optics. *Rev. Mod. Phys.* **92**, 035005 (2020).

39. Roslund, J., De Araujo, R. M., Jiang, S., Fabre, C. & Treps, N. Wavelength-multiplexed quantum networks with ultrafast frequency combs. *Nat. Photonics* **8**, 109–112 (2014).

40. Cai, Y. et al. Multimode entanglement in reconfigurable graph states using optical frequency combs. *Nat. Commun.* **8**, 15645 (2017).

41. Treps, N., Delaubert, V., Maitre, A., Courty, J. & Fabre, C. Quantum noise in multipixel image processing. *Phys. Rev. A* **71**, 013820 (2005).

42. Lamine, B., Fabre, C. & Treps, N. Quantum improvement of time transfer between remote clocks. *Phys. Rev. Lett.* **101**, 123601 (2008).

43. Su, X. et al. Gate sequence for continuous variable one-way quantum computation. *Nat. Commun.* **4**, 2828 (2013).

44. Ukai, R. et al. Demonstration of unconditional one-way quantum computations for continuous variables. *Phys. Rev. Lett.* **106**, 240504 (2011).

45. Menicucci, N. C., Flammia, S. T. & Pfister, O. One-way quantum computing in the optical frequency comb. *Phys. Rev. Lett.* **101**, 130501 (2008).

46. Andersen, U. L., Neergaard-Nielsen, J. S., van Loock, P. & Furusawa, A. Hybrid discrete- and continuous-variable quantum information. *Nat. Phys.* **11**, 713–719 (2015).

47. Braunstein, S. L. Squeezing as an irreducible resource. *Phys. Rev. A* **71**, 055801 (2005).

48. Ferrini, G., Gazeau, J. P., Coudreau, T., Fabre, C. & Treps, N. Compact Gaussian quantum computation by multi-pixel homodyne detection. *N. J. Phys.* **15**, 093015 (2013).

49. Cai, Y., Xiang, Y., Liu, Y., He, Q. Y. & Treps, N. Versatile multipartite Einstein-Podolsky-Rosen via a quantum frequency comb. *Phys. Rev. Res.* **2**, 032046(R) (2020).

50. Ra, Y. et al. Non-Gaussian quantum states of a multi- mode light field. *Nat. Phys.* **16**, 144–147 (2020).

AUTHOR CONTRIBUTIONS

Y.C. and J.R. performed the experiments; Y.C., J.R., and V.T. did the theoretical analysis; C.F. and N.T. supervised the work. All authors contributed to writing of the paper.

COMPETING INTERESTS

The authors declare no competing interests.

ADDITIONAL INFORMATION

Correspondence and requests for materials should be addressed to Y.C. or N.T.

Reprints and permission information is available at http://www.nature.com/reprints

Publisher's note Springer Nature remains neutral with regard to jurisdictional claims in published maps and institutional affiliations.